Rapid erosion increases the efficiency of hillslope sediment transport

E. J. Gabet[1], S. M. Mudd[2], R. W. Wood[1], S. W. D. Grieve[3], S. A. Binnie[4], T. J. Dunai[4]

[1] Department of Geology, San Jose State University, San Jose, California, 95192, USA.
[2] School of Geosciences, University of Edinburgh, Edinburgh, UK, EH9 3FE.
[3] School of Geography, Queen Mary University of London, London, UK, E1 4NS.
[4] Institute for Geology and Mineralogy, University of Cologne, Germany, 50674.

Corresponding author: Emmanuel Gabet (manny.gabet@sjsu.edu)

Key Points:

- The transport efficiency of soil creep processes increases with erosion rate
- The increase in transport efficiency in rapidly eroding landscapes may be due to larger soil particles
- There may be an unrecognized dilational soil creep process that dominates hillslope transport

Abstract

Processes contributing to soil creep dominate the downslope movement of soil particles in many regions, and climate is generally hypothesized to have an important influence on the efficiency of these processes. However, a lack of uniformity in the measurement of transport efficiency has been an obstacle to evaluating the controls on this important landscape parameter. We address this problem by using a single method for calculating transport efficiency from 1-m LiDAR digital elevation data for a set of 6 regions in the United States with a broad range of mean annual precipitation (555 – 1405 mm), mean annual temperature (2 – 15 °C), and erosion rates (6 – 922 mm/ky). To further ensure consistency, the erosion rates are calculated from *in-situ* cosmogenic ^{10}Be concentrations using the same algorithm, and a single source is used for the climate data. Surprisingly, transport efficiency appears to be insensitive to climate but strongly dependent on erosion rate. We propose that this

relationship arises from the longer path lengths of the coarser particles found in the soils of rapidly eroding landscapes. Our results imply that the time necessary for a landscape to regain topographic steady-state after a change in erosion rate will depend on the direction of that change. Moreover, our results suggest that there may be a dilational soil creep process that has yet to be identified.

Index Terms: 1826, 1819, 1862

1. Introduction

On soil-mantled surfaces too gentle for significant landsliding, particles are primarily transported downslope by soil creep. Soil creep is a general term for the cumulative effect of myriad individual processes that locally disturb soil, such as the freezing and thawing of pore water [*Anderson et al.*, 2013], shrink-swell cycles [*Carson and Kirkby*, 1972], dry ravel [*Anderson et al.*, 1959; *Gabet*, 2003], burrowing by animals [*Gabet et al.*, 2003], and tree throw [e.g., *Denny and Goodlett*, 1956]. Culling [1963] proposed that the rate of soil creep (q_s; L^2 T^{-1}) is linearly proportional to hillslope gradient, S (L L^{-1}), such that

$$q_s = DS \tag{1}$$

where D (L^2 T^{-1}) is a sediment transport coefficient. The sediment transport coefficient, D, is a measure of the efficiency of the various soil creep processes, and its magnitude sets the pace for hillslope evolution [e.g., *Fernandes and Dietrich*, 1997; *Roering et al.*, 1999]. Although a nonlinear relationship between gradient and flux is supported by topographic analysis [*Andrews and Bucknam*, 1987; *Grieve et al.*, 2016; *Hurst et al.*, 2012; *Roering et al.*, 1999] and physical simulations [*Gabet*, 2003; *Roering et al.*, 2001], this relationship reduces to Eqn. (1) on slopes < 20° [*Hurst et al.*, 2012].

Our understanding of the large-scale controls on *D* for a particular landscape is limited. Because soil creep processes are typically climatically controlled, either directly (e.g., freeze-thaw) or indirectly through climate's effect on the distribution of the biota, temperature and precipitation are expected to have a dominant role in the transport efficiency of soil creep [e.g., *Dunne et al.*, 2010; *Hanks*, 2000; *Pelletier et al.*, 2011]. Indeed, Hurst et al. [2013] and Richardson et al. [2019] found that *D* increases with mean annual precipitation, albeit weakly; the latter also found that *D* increases with the aridity index, which is the ratio between precipitation and evapotranspiration [*Trabucco and Zomer*, 2019]. In contrast, Ben-Asher et al. [2017] concluded that transport efficiency decreases with precipitation, although this result was based on a small data set. Soil thickness [*Furbish et al.*, 2009; *Heimsath et al.*, 2005] and soil texture [*Furbish et al.*, 2009], as well as underlying lithology [*Hurst et al.*, 2013], may also be important factors. A lack of uniformity in measuring *D*¸ however, has been an obstacle in investigating the effect of these various factors [*Hurst et al.*, 2013; *Richardson et al.*, 2019].

Determining the controls on the transport coefficient is important for a variety of reasons. Because many landscapes are soil-mantled, not affected by overland flow, and too gentle for significant landsliding, Eqn. (1) and its nonlinear counterpart offer a complete description (or nearly so) of sediment transport across much of the Earth's surface. In addition, the magnitude of *D* controls the flux of sediment delivered to the fluvial system [e.g., *Reid and Dunne*, 1996], and it determines how rapidly a landscape can recover to a steady-state topography after a change in the rate of baselevel lowering [*Fernandes and*

Dietrich, 1997]. Moreover, studies have used Eqn. (1) and its nonlinear version to model the degradation of fault scarps to estimate earthquake recurrence interval [e.g., *Hanks and Schwartz*, 1987], and the results are sensitive to the value of the transport coefficient. Finally, understanding the role of the various factors on D is important as geologists attempt to infer erosion rates based on topographic analyses [*Hurst et al.*, 2012]. In this contribution, we gauge the influence of various factors on the efficiency of sediment transport by soil creep using, for the first time, uniform methods to measure D across a range of climatic conditions.

2. Methods

2.1. Site selection and descriptions

Appropriate sites were limited to watersheds which had both LiDAR and cosmogenic ^{10}Be data sets. The ^{10}Be data came from a global compilation [*Harel et al.*, 2016], and the associated LiDAR data were acquired from the OpenTopography (http://opentopo.sdsc.edu) and USGS (https://viewer.nationalmap.gov) platforms. LiDAR data with spatial resolutions below 1-m cannot accurately resolve ridgeline curvatures in all settings [*Grieve et al.*, 2016] and so any sites without 1-m resolution data were excluded from the analysis. Because ridgeline curvatures were used to estimate D (see below), only watersheds that appeared to be in topographic steady-state were chosen. For example, watersheds with clear knickpoints or with asymmetrical ridges were avoided, as well as steep watersheds advancing into low-relief surfaces. Simulations of hillslope evolution suggest that hillslopes with declining erosion rates adjust so quickly that they are difficult to differentiate from steady state hillslopes and, further, hillslopes experiencing accelerated uplift only preserve the signature of changing erosion rates for tens of thousands of years [*Mudd*, 2017]. Therefore, by avoiding areas with obvious signs of landscape transience, we are unlikely to find ridgeline curvatures reflective of transient conditions. Thirty sites from six regions in the United States met our criteria: the Olympic Peninsula (WA), the Feather River area (CA), the San Gabriel Mountains (CA), Yucaipa Ridge (CA), the Idaho Plateau (ID), and the Blue Ridge Mountains (VA) (Figure 1). Some of the regions (e.g., the San Gabriel Mountains) had ^{10}Be data at sites not covered by available LiDAR data and, thus, their full data-sets could not be used.

From the 800-m resolution PRISM climate data [*PRISM*, 2014], recent (1981 – 2010) 30-yr means for annual precipitation (MAP) and annual temperature (MAT) range from 560 – 3200 mm/y and 2 – 15 °C, respectively, within our set of sites. The aridity index varies from 814 – 2037 [*Trabucco and Zomer*, 2019]. While these data are for the modern climate, we assume that they are representative (at least in a relative sense) of the climate state over the time-scale of the erosion rates measured with ^{10}Be (i.e., 10^3 - 10^5 yrs). All watersheds but one are underlain by quartz-rich bedrock (i.e., plutonic rocks and sandstone). Climate data, geographical coordinates, and bedrock type for each site are presented in Table 1.

On the basis of vegetation community, our field observations, and published accounts, we can infer the primary disturbance-driven soil creep processes at each site. Transport at sites in the forested regions (Olympic Peninsula, Feather River, Blue Ridge Mountains, and the Idaho Plateau) is likely dominated by tree-throw, root growth-and-decay, and burrowing by invertebrates [*Denny and Goodlett*, 1956; *Gabet et al.*, 2003; *Hurst et al.*, 2013; *Wood*, 2013]. Rainsplash is likely to be an important contributor to disturbance-driven creep at the more arid sites (San Gabriel Mountains and Yucaipa Ridge) because they have little ground-cover and generally shrubby vegetation [*Dunne and Malmon*, 1999]; dry ravel might also contribute, although it is unlikely to be an important process on the gentle slopes analyzed here [*Gabet*, 2003; *Lamb et al.*, 2011].

2.2. Erosion rate calculations

To ensure a consistent method for calculating erosion rates, they were determined from ^{10}Be concentrations in detrital quartz grains (Table 1). For five of the study regions, published ^{10}Be concentrations were used to calculate basin-scale erosion rates. For the Idaho Plateau sites, ^{10}Be concentrations were measured from soil and fluvial sediment samples collected for this study (see below). For all six study regions, erosion rates were calculated from the ^{10}Be concentrations using a single algorithm [*Mudd et al.*, 2016].

A full description of the Idaho Plateau field area can be found in Wood [2013]. Ridgetop and basin-scale denudation rates were determined by measuring cosmogenic ^{10}Be concentrations in quartz [*Brown et al.*, 1995; *Granger et al.*, 1996]. The ridgetop rates were determined from regolith samples taken from the top 20 cm of three soil pits. For the basin-scale erosion rates, fluvial sediment was taken from three 1st-order streams. Pure quartz fractions from the crushed and sieved (250-710 μm) and magnetically separated samples were obtained using published procedures [*Mifsud et al.*, 2013; *Nishiizumi et al.*, 2007]. ICP-OES analysis of purity was undertaken on splits of the etched quartz. Samples were spiked with ~200 μg of a commercial Be carrier (Scharlab Berylium ICP standard solution) and prepared as AMS targets at the University of Cologne using a standard sample preparation method [2015]. The samples were prepared alongside a reagent blank; ^{10}Be concentrations following blank subtraction are reported in Table DR2. Blank corrections are <2 %, except for sample S2, for which the correction is <5 %. Samples were measured on CologneAMS [*Dewald et al.*, 2013] and normalized to reference standards [2007]. Uncertainties in the concentrations are estimated by propagating the uncertainties of the AMS measurements and mass of Be added during spiking (estimated 1σ uncertainty of 1%) of both the samples and the blank.

^{10}Be concentrations were converted to denudation rates with the CAIRN software package, which accounts for topographic shielding and snow shielding [*Mudd et al.*, 2016]. We calculated snow shielding by first fitting a bilinear trend in snow water equivalent (SWE) as a function of elevation based on regional climate data from the National Oceanic and Atmospheric Association [*NOAA*, 2016] and following Kirchner et al. [2014]. SWE averages were converted to snow shielding values by assuming that snow reduces production solely by spallation [*Mudd et al.*, 2016]. Snow shielding is highly uncertain because of the difficulty of estimating the average SWE over the last several thousand years, which is the averaging timescale for ^{10}Be [e.g., *Lal*, 1991]. We calculated denudation rates with no snow shielding to assess the sensitivity of denudation rate to snow thickness and found that, without accounting for snow, denudation rate estimates could be as much as 15% higher (for sample S3) but, for most samples, the differences were less than 10%.

2.3. Transport Coefficient Calculations

Direct estimates of the transport efficiency by field measurements of sediment fluxes over the relevant time and spatial scales across a range of landscapes is impractical. Instead, along ridgelines, where slopes are gentle and soil creep is well described by Eqn. (1), the transport coefficient can be calculated with

$$D = -\left(\frac{E}{C_{HT}}\right)\left(\frac{\rho_r}{\rho_s}\right) \qquad (2)$$

where E is the erosion rate (L T^{-1}), C_{HT} (L^{-1}) is the ridgecrest's two-dimensional curvature (i.e., the Laplacian of elevation), and ρ_s and ρ_r are the density (L^3T^{-1}) of soil and rock, respectively [*Roering et al.*, 2007]. The ratio ρ_r/ρ_s was assumed to be 2 [*Hurst et al.*, 2012]; this value is probably only approximately correct for each of our sites and likely varies by ±25%. Ridgeline curvatures were calculated from a 1-m LiDAR DEM for each site using a six-term polynomial function to fit the elevation data within a circular sliding window with a diameter of 12 m [*Hurst et al.*, 2012]. The second derivative of the polynomial function at the window's center is that cell's two-dimensional curvature. Because topographic noise could produce outliers, the median of the curvatures along each watershed's ridgeline was used in our analyses [*Hurst et al.*, 2012]. The average slopes (± 1σ) along the ridgelines ranged from 0.5 ± 3° (Blue Ridge Mtns) to 9 ± 6° (Yucaipa Ridge), thereby validating the use of Eqn. 1. Note that, even at the steepest site along Yucaipa Ridge, nearly 95% of the area analyzed had slopes < 20°. Finally, an automated procedure was used to detect the presence of bedrock outcrops along the ridgelines [*Milodowski et al.*, 2015] to confirm that the sites were mantled with soil. One Yucaipa Ridge site had 75% soil-cover and the other had 90% soil-cover; the soil-cover at the other sites ranged from 97 – 100%.

3. Results

The transport efficiency is not correlated with any of the climate parameters (Figure 2) nor with the 'effective energy and mass transfer' variable (not shown), a parameter which incorporates both MAT and MAP to represent the influence of climate on soil processes [*Rasmussen and Tabor*, 2007]. We find, however, that hilltop curvature is strongly dependent on the square root of erosion rate (Figure 3) which implies, from Eqn. (2), that D is also proportional to $E^{1/2}$ (Figure 4).

We performed Monte Carlo simulations to assess whether the square root relationship between C and E could have arisen purely by chance. For each region, we assumed that a single value of D represents the transport efficiency, which is reasonable considering that soil creep processes should be similar at sites in proximity to each other. Thus, for each of the six regions, a value for D was randomly chosen from a normal distribution with an average of 0.0072 ± 0.0062 m^2/yr; these are the mean and 1σ of the coefficient values for each region (Table 1). For each of the thirty sites, a curvature was calculated according to Eqn. (2) with the randomly chosen D and the measured E. A power-law regression was then fit through the 30 pairs of erosion rate and synthetic curvature values, and the exponent and R^2 values were recorded. This process was repeated 10,000 times. Figure 5, a plot of the power-law exponents and their associated R^2 values, suggests that the $|C_{HT}| \propto E^{1/2}$ relationship is highly unlikely (i.e., < 0.01% probability) to have arisen by chance with an R^2 of 0.83.

4. Discussion

The important role of erosion rate on the efficiency of hillslope sediment transport and the insignificance of climate is unexpected considering that others have found climate to be a weak but determining factor in the value of D [*Hurst et al.*, 2013; *Richardson et al.*, 2019]. Richardson et al. [2019] present data similar to ours in which erosion rates were determined with cosmogenic isotopes, hilltop curvature was extracted from 1-m DEMs, and transport efficiency was calculated from Eqn. (2). Although their procedure for calculating curvature is different from ours and, thus, their results are not directly comparable to ours, our analysis of their data also reveals a robust relationship between D and erosion rate (Figure 6).

To explore how transport efficiency might increase with erosion rate, the factors contributing to soil creep can be assessed with two approaches. For discrete, intermittent large-scale soil creep events (e.g., tree throw), the transport efficiency can be calculated as

$$D = f_e \overline{V} \overline{d} \tag{3}$$

where f_e is the frequency of events per unit area ($T^{-1}L^{-2}$), $\overline{V}$ is the average volume (L^3) of soil displaced with each event, and $\overline{d}$ is the average distance (L) that volume of soil is displaced [*Gabet*, 2000]. For example, in the case of tree throw, the transport coefficient will depend on the number of toppled trees over a period of time, the average volume of soil in the root plates, and the distance that the root plates are displaced [*Gabet et al.*, 2003]. We are not aware of any reason why any of these three factors would increase with erosion rate. Indeed, in the case of bioturbation, $\overline{V}$, f_e, and A_f might be expected to *decrease*. For example, because soils tend to be thinner where erosion rates are high [*Gabet et al.*, 2015], the volume of soil available for transport by three throw should decrease. In addition, the frequency of bioturbation might be expected to decrease in rapidly eroding landscapes because of lower plant biomass [*Milodowski et al.*, 2014].

For dilational creep processes in which soil particles are lofted up and then settle down due to gravity, D can be expressed as [*Furbish et al.*, 2009]

$$D = kRh\overline{N_a\left(1-\frac{C}{C_m}\right)^2}\cos^2\theta \tag{4}$$

where k is an empirically determined dimensionless constant that accounts for particle shape and the relationship between mean free path length and the vertical displacement of particles, R is particle radius (L), h is soil thickness (L), C is particle concentration (L^3L^{-3}), C_m is the maximum value of C, N_a is the particle activation rate (T^{-1}), θ is the hillslope angle (°) (equal to zero at the ridgecrest), and the overbar signifies vertically averaged quantities. The particle concentration (a function of soil bulk density) is not likely to be dependent on erosion rate to a significant degree and, if it is, the term in parentheses would likely decrease with increasing erosion rate, thereby suppressing the value of D. Also we find no reason to suspect that the particle activation rate would increase with erosion rate, particularly where bioturbation is an important soil creep process. Indeed, the only variables in Eqn. 4 known to vary systematically and significantly with erosion rate are soil thickness [*Heimsath et al.*, 1999], h, and particle size, R *[Attal et al., 2014]*.

To explore the potential role of soil thickness on the transport coefficient, we hold the other variables in Eqn. 4 constant to yield

$$D \propto k' hR \qquad (5)$$

where k' (T^{-1}) incorporates k from Eqn. 4 as well as factors such as particle concentration [*Furbish et al.*, 2009]. Equation 2, which relates hilltop curvature to erosion rate, can be simplified as

$$E \propto D|C_{HT}| \qquad (6).$$

Because hilltop curvatures are negative, their absolute values are used here for clarity, rather than incorporating a 'minus' sign (compare with Eqn. 2). Combining the regression from Figure 3

$$|C_{HT}| \propto E^{1/2} \qquad (7)$$

with Eqns. (5) and (6) and assuming that k' does not vary significantly with erosion rate produces

$$hR \propto E^{1/2} \qquad (8).$$

To satisfy Eqn. (8), either *h* or *R*, or both, must increase with erosion rate. If we assume that *R* is not a function of erosion rate (we will revisit this below), then *h* would need to increase with erosion rate, a result contradicted by field evidence [e.g., *Gabet et al.*, 2015]. Therefore, the thinner soils in rapidly eroding landscapes cannot account for the increase in transport efficiency with erosion rate.

In contrast, particle size is known to increase with erosion rate [*Attal et al.*, 2014; *Riebe et al.*, 2015]; where erosion is slow, particles are exposed to weathering processes for longer periods of time because the thicker soils and the slower lowering of the soil surface yields longer soil residence times for the particles [e.g., *Mudd and Yoo*, 2010]. Particle size is a factor in the transport coefficient (Eqn. 4) because it controls the mean free path of particles in a soil creeping by dilational processes [*Furbish et al.*, 2009]. Indeed, laboratory experiments have demonstrated that, for the same input of energy, coarse-grained soils will creep faster than fine-grained soils [*Deshpande et al.*, 2020]. In addition, of the various factors that could affect the rate of soil creep, mean particle size is the one with the most potential to vary by multiple orders-of-magnitude between watersheds eroding at different rates [*Marshall and Sklar*, 2012].

While particle size is a potential candidate for explaining the relationship between transport efficiency and erosion rate found here, this raises two perplexing issues. First, the hypothesis that R is the determining factor in the difference in transport efficiency between our sites implies that soil creep at the six study regions is dominated by the same dilational process. Since the biotic communities vary widely between the study regions (temperate rainforest to semi-arid chaparral), this dilational process is likely abiotic. Moreover, the lack of a relationship found here between D and precipitation (Figure 2B), and the weak relationship between the two presented elsewhere [*Hurst et al.*, 2013; *Richardson et al.*, 2019], argue against shrink-swell as a likely candidate for this dilational process. The alignment of sites from all six regions along the same trendline (Figure 4), therefore, suggests that there is an important yet unrecognized dilational soil creep process that is abiotic and, at best, only weakly dependent on climate. Second, because the more rapid weathering rates in wetter climates should lead to smaller soil particles [*Marshall and Sklar*, 2012], the transport coefficient should decrease in wetter climates. However, as noted earlier, D has been found to increase with precipitation, albeit weakly [*Hurst et al.*, 2013; *Richardson et al.*, 2019].

We considered the effect of topographic stresses on the creation of fractures as an alternative explanation for our results [*Clair et al.*, 2015; *Miller and Dunne*, 1996]. The greater ridgeline curvatures in the rapidly eroding landscapes could be driving the development of more bedrock fractures which would accelerate weathering processes and create a thicker layer of mobile regolith than would otherwise be predicted by the erosion rate [*Pelletier*, 2017]. This explanation, however, is unlikely. The tectonic stress regime is an important contributor to topographic stresses and, whereas the tectonic stress in the Feather River region is extensional, it is compressional in the San Gabriel Mountains region [*Zoback*, 1992], yet their data overlap (Figures 3, 4).

Although we are unable to explain conclusively why the transport efficiency increases with erosion rate, this relationship has important implications. Our results suggest that the pace at which steady-state topography is restored after a change in erosion rate will depend on the direction of that change. For example, the increase in transport efficiency accompanying an acceleration in erosion rate will hasten the return to steady-state; in contrast, a slowing of the erosion rate will depress the transport efficiency and delay the return to equilibrium conditions. In addition, the robust relationship between the ridgetop curvature and erosion rate across a range of climatic conditions suggests that the latter can be estimated directly from topographical analysis in landscapes similar to those analyzed in this study. However, erosion rates determined with this procedure must incorporate uncertainties in the original ^{10}Be erosion rate measurements, uncertainties in the curvature measurements (expressed as the median absolute deviation), and the uncertainty in the regression, and we have not yet found a satisfactory approach to this problem. Nevertheless, this method has the potential for providing a simple approach for estimating watershed-scale erosion rates through the measurement of hilltop curvatures.

5. Conclusions

Using a single method for estimating values of *D*, the measure of hillslope transport efficiency, provides an opportunity to detect the factors influencing this critical variable landscape variable. By combining erosion rates calculated with ^{10}Be concentrations with measurements of hilltop curvature from 1-m DEMs, we find that D increases with erosion rate. After exploring possible explanations for this result, we conclude that larger particle sizes in rapidly eroding terrain may lead to more efficient hillslope transport due to longer path lengths. An intriguing consequence of this conclusion is the implication that an unrecognized abiotic dilational process, perhaps only weakly dependent on climate, dominates soil creep in our study regions.

Acknowledgments

Idaho field work for this project was conducted with assistance from B. Wood, S. Powell, and E. Hewitt. There were no real or perceived financial conflicts of interest for any author nor did any author have an affiliation that could be perceived as having a conflict of interest with respect to the results of this paper. The data supporting the conclusions can be found in the tables and references. This project was partially funded by graduate student research grants from GSA and SJSU. LiDAR elevation data were acquired with a Seed Project from the National Center for Airborne Laser Mapping in the summer of 2011. Software used for analysis was developed under NERC grant NE/J009970/1. We are grateful to J. Pelletier and D. Furbish for extended and insightful discussions.

Data Availability Statement

Datasets for this research, and their sources, are provided in Table 1.

References

Anderson, H. W., G. B. Coleman, and P. J. Zinke (1959), Summer slides and winter scour, dry-wet erosion in Southern California mountains: U.S.D.A., Forest Service, *Pacific Southwest Forest and Range Experiment Station Technical Paper PSW-36*.

Anderson, R. S., S. P. Anderson, and G. E. Tucker (2013), Rock damage and regolith transport by frost: An example of climate modulation of the geomorphology of the critical zone, *Earth Surface Processes and Landforms*, *38*(3), 299-316.

Andrews, D. J., and R. C. Bucknam (1987), Fitting degradation of shoreline scarps by a nonlinear diffusion model, *Journal of Geophysical Research*, *92*(B12), 12,857-812,867.

Attal, M., S. M. Mudd, M. D. Hurst, B. Weinman, K. Yoo, and M. Naylor (2014), Impact of change in erosion rate and landscape steepness on hillslope and fluvial sediments grain size in the Feather River Basin (Sierra Nevada, California), *Earth Surface Dynamics*, *2*, 1047-1092.

Ben-Asher, M., I. Haviv, J. J. Roering, and O. Crouvi (2017), The influence of climate and microclimate (aspect) on soil creep efficiency: Cinder cone morphology and evolution along the eastern Mediterranean Golan Heights, *Earth Surface Processes and Landforms*, *42*(15), 2649-2662.

Binnie, S. A., T. J. Dunai, E. Voronina, T. Goral, S. Heinze, and A. Dewald (2015), Separation of Be and Al for AMS using single-step column chromatography, *Nuclear Instruments and Methods in Physics Research Section B: Beam Interactions with Materials and Atoms*, *361*, 397-401.

Brown, E. T., R. F. Stallard, M. C. Larsen, G. M. Raisbeck, and F. Yiou (1995), Denudation rates determined from the accumulation of in situ-produced 10Be in the Luquillo Experimental Forest, Puerto Rico, *Earth and Planetary Science Letters*, *129*(1-4), 193-202.

Carson, M. A., and M. J. Kirkby (1972), *Hillslope form and process*, 475 pp., Cambridge University Press, New York.

Clair, J. S., S. Moon, W. S. Holbrook, J. T. Perron, C. S. Riebe, S. J. Martel, B. Carr, C. Harman, K. Singha, and D. d. Richter (2015), Geophysical imaging reveals topographic stress control of bedrock weathering, *Science*, *350*, 534-538.

Culling, W. E. H. (1963), Soil creep and the development of hillside slopes, *Journal of Geology*, *71*, 127-161.

Denny, C., and J. Goodlett (1956), Microrelief resulting from fallen trees, *USGS Professional Publication*, *288*, 59-68.

Deshpande, N., D. J. Furbish, P. Arratia, and D. Jerolmack (2020), The perpetual fragility of creeping hillslopes, *EarthArXiv*, *doi:10.31223/osf.io/qc9jh*.

Dewald, A., et al. (2013), CologneAMS, a dedicated center for accelerator mass spectrometry in Germany, *Nuclear Instruments and Methods in Physics Research Section B: Beam Interactions with Materials and Atoms*, *294*, 18-23.

Dunne, T., and D. Malmon (1999), Rainsplash transport and hillslope evolution, *manuscript in preparation*.

Dunne, T., D. V. Malmon, and S. M. Mudd (2010), A rain splash transport equation assimilating field and laboratory measurements, *Journal of Geophysical Research - Earth Surface*, *115*(F01001), 1-16.

Fernandes, N. F., and W. E. Dietrich (1997), Hillslope evolution by diffusive processes: the timescale for equilibrium adjustments, *Water Resources Research*, *33*(6), 1307-1318.

Furbish, D. J., P. K. Haff, W. E. Dietrich, and A. M. Heimsath (2009), Statistical description of slope-dependent soil transport and the diffusion-like coefficient, *Journal of Geophysical Research*, *114*(F00A05), doi:10.1029/2009JF001267.

Gabet, E. J. (2000), Gopher bioturbation: Field evidence for nonlinear hillslope diffusion, *Earth Surface Processes and Landforms*, *25*(13), 1419-1428.

Gabet, E. J. (2003), Sediment transport by dry ravel, *Journal of Geophysical Research*, *108*(B1), 2050, 2010.1029/2001JB001686.

Gabet, E. J., O. J. Reichman, and E. Seabloom (2003), The effects of bioturbation on soil processes and sediment transport, *Annual Review of Earth and Planetary Sciences*, *31*, 259-273.

Gabet, E. J., S. M. Mudd, D. T. Milodowski, K. Yoo, M. D. Hurst, and A. Dosseto (2015), Local topography and erosion rate control regolith thickness along a ridgeline in the Sierra Nevada, California, *Earth Surface Processes and Landforms*, *40*(13), 1779-1790.

Granger, D. E., J. W. Kirchner, and R. C. Finkel (1996), Spatially averaged long-term erosion rates measured from in situ-produced cosmogenic nuclides in alluvial sediment, *Journal of Geology*, *104*(3), 249-257.

Grieve, S. W. D., S. M. Mudd, and M. D. Hurst (2016), How long is a hillslope?, *Earth Surface Processes and Landforms*, *41*(8), 1039-1054.

Hanks, T. C. (2000), The age of scarplike landforms from diffusion-equation analysis, *Quaternary Geochronology: Methods and Applications*, 313-338.

Hanks, T. C., and D. P. Schwartz (1987), Morphologic dating of the pre-1983 fault scarp on the Lost River Fault at Doublespring Pass Road, Custer County, Idaho, *Bulletin of the Seismological Society of America*, *77*, 837-846.

Harel, M. A., S. M. Mudd, and M. Attal (2016), Global analysis of the stream power law parameters based on worldwide 10Be denudation rates, *Geomorphology*, *268*, 184-196.

Heimsath, A. M., D. J. Furbish, and W. E. Dietrich (2005), The illusion of diffusion: Field evidence for depth-dependent sediment transport, *Geology*, *33*(12), 949-952.

Heimsath, A. M., W. E. Dietrich, K. Nishiizumi, and R. C. Finkel (1999), Cosmogenic nuclides, topography, and the spatial variation of soil depth, *Geomorphology*, *27*, 151-172.

Hurst, M. D., S. M. Mudd, R. C. Walcott, M. Attal, and K. Yoo (2012), Using hilltop curvature to derive the spatial distribution of erosion rates, *Journal of Geophysical Research - Earth Surface*, *115*, 1-19.

Hurst, M. D., S. M. Mudd, K. Yoo, M. Attal, and R. C. Walcott (2013), Influence of lithology on hillslope morphology and response to tectonic forcing in the northern Sierra Nevada of California, *Journal of Geophysical Research - Earth Surface*, *118*, 832-851.

Kirchner, P. B., R. C. Bales, N. P. Molotoch, J. Flanagan, and Q. Guo (2014), LiDAR measurement of seasonal snow accumulation along an elevation gradient in the southern Sierra Nevada, California, *Hydrological Earth Systems Science*, *18*, 4261-4275.

Lal, D. (1991), Cosmic ray labeling of erosion surfaces: In situ nuclide production rates and erosion models, *Earth and Planetary Science Letters*, *104*(24), 424-439.

Lamb, M. P., J. S. Scheingross, W. H. Amidon, E. Swanson, and A. Limaye (2011), A model for fire-induced sediment yield by dry ravel in steep landscapes, *Journal of Geophysical Research*, *116*(F03006), doi: 10.1029/2010JF001878.

Marshall, J. A., and L. S. Sklar (2012), Mining soil databases for landscape-scale patterns in the abundance and size distribution of hillslope rock fragments, *Earth Surface Processes and Landforms*, *37*(3), 287-300.

Mifsud, C., T. Fujioka, and D. Fink (2013), Extraction and purification of quartz in rock using hot phosphoric acid for in situ cosmogenic exposure dating, *Nuclear Instruments and Methods in Physics Research Section B: Beam Interactions with Materials and Atoms*, *294*, 203-207.

Miller, D. J., and T. Dunne (1996), Topographic perturbations of regional stresses and consequent bedrock fracturing, *Journal of Geophysical Research*, *101B*, 25,523-525,536.

Milodowski, D. T., S. M. Mudd, and E. T. Mitchard (2014), Erosion rates as a potential bottom-up control of forest structural characteristics in the Sierra Nevada Mountains, *Ecology*, *96*(1), 31-38.

Milodowski, D. T., S. M. Mudd, and E. T. A. Mitchard (2015), Topographic roughness as a signature of the emergence of bedrock in eroding landscapes, *Earth Surf. Dynam.*, *3*(4), 483-499.

Mudd, S. M. (2017), Detection of transience in eroding landscapes, *Earth Surface Processes and Landforms*, *42*(1), 24-41.

Mudd, S. M., and K. Yoo (2010), Reservoir theory for studying the geochemical evolution of soils, *Journal of Geophysical Research: Earth Surface*, *115*(F03030).

Mudd, S. M., M. Harel, M. D. Hurst, S. W. D. Grieve, and S. M. Marrero (2016), The CAIRN method: Automated, reproducible calculation of catchment-averaged denudation rates from cosmogenic radionuclide concentrations, *Earth Surface Dynamics*, *4*, 655-674.

Nishiizumi, K., M. Imamura, M. W. Caffee, J. R. Southon, R. C. Finkel, and J. McAninch (2007), Absolute calibration of 10be AMS standards, *Nuclear Instruments and Methods in Physics Research Section B: Beam Interactions with Materials and Atoms*, *258*(2), 403-413.

NOAA (2016), National Center for Environmental Information, edited.

Pelletier, J. D. (2017), Quantifying the controls on potential soil production rates: a case study of the San Gabriel Mountains, California, *Earth Surf. Dynam.*, *5*(3), 479-492.

Pelletier, J. D., et al. (2011), Calibration and testing of upland hillslope evolution models in a dated landscape: Banco Bonito, New Mexico, *Journal of Geophysical Research: Earth Surface*, *116*(F4).

PRISM (2014), PRISM Climate Group, edited.

Rasmussen, C., and N. Tabor (2007), Applying a quantitative pedogenic energy model across a range of environmental gradients, *Soil Science Society of America Journal*, *71*(6), 1719-1729.

Reid, L. M., and T. Dunne (1996), *Rapid evaluation of sediment budgets*, 164 pp., Catena Verlag, Germany.

Richardson, P. W., J. T. Perron, and N. D. Schurr (2019), Influences of climate and life on hillslope sediment transport, *Geology*, *47*, 423-426.

Riebe, C. S., L. S. Sklar, C. E. Lukens, and D. L. Shuster (2015), Climate and topography control the size and flux of sediment produced on steep mountain slopes, *Proceedings of the National Academy of Sciences*, *112*(51), 15574-15579.

Roering, J. J., J. W. Kirchner, and W. E. Dietrich (1999), Evidence for non-linear, diffusive sediment transport on hillslopes and implications for landscape morphology, *Water Resources Research*, *35*(3), 853-870.

Roering, J. J., J. T. Perron, and J. W. Kirchner (2007), Functional relationships between denudation and hillslope form and relief, *Earth and Planetary Science Letters*, *264*(1), 245-258.

Roering, J. J., J. W. Kirchner, L. S. Sklar, and W. E. Dietrich (2001), Hillslope evolution by nonlinear creep and landsliding: An experimental study, *Geology*, *29*(2), 143-146.

Trabucco, A., and R. Zomer (2019), *Global Aridity Index and Potential Evapotranspiration (ET0) Climate Database v2*.

Wood, R. (2013), Transient hillslope response to an incision wave sweeping up a watershed: a case study from the Salmon River, MS thesis, 42 pp, San Jose State University, San Jose, CA.

Zoback, M. L. (1992), First- and second-order patterns of stress in the lithosphere: The World Stress Map Project, *Journal of Geophysical Research: Solid Earth*, *97*(B8), 11703-11728.

FIGURES

Figure 1. Map of the United States with study regions marked with a star. WA = Washington; IP = Idaho Plateau; FR = Feather River; SGM = San Gabriel Mountains; YR = Yucaipa Ridge; VA = Virginia.

(a)

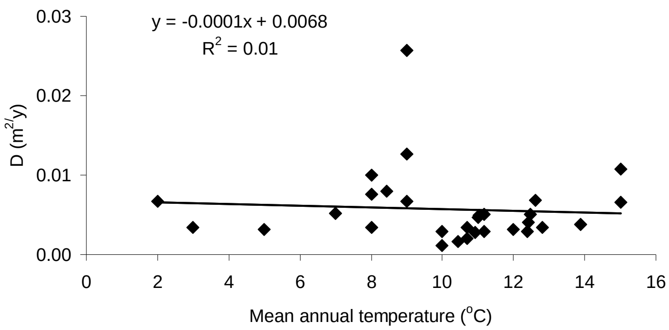

(b)

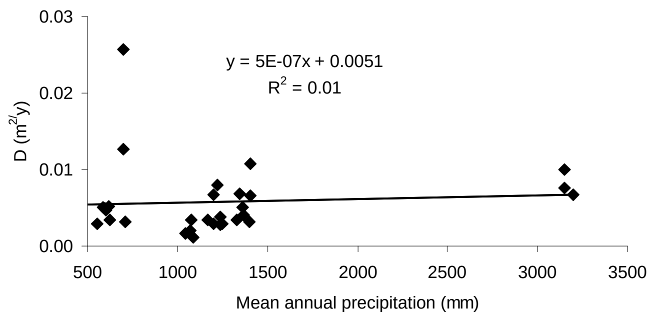

(c)

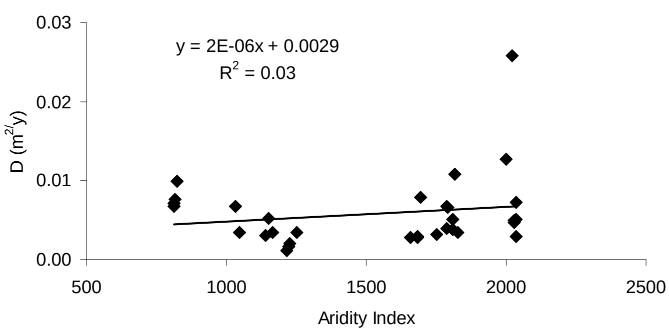

Figure 2. Transport efficiency vs. climatic parameters. *D* does not vary according to (a) mean annual temperature, (b) mean annual precipitation, or (c) the aridity index. Straight lines are linear regressions.

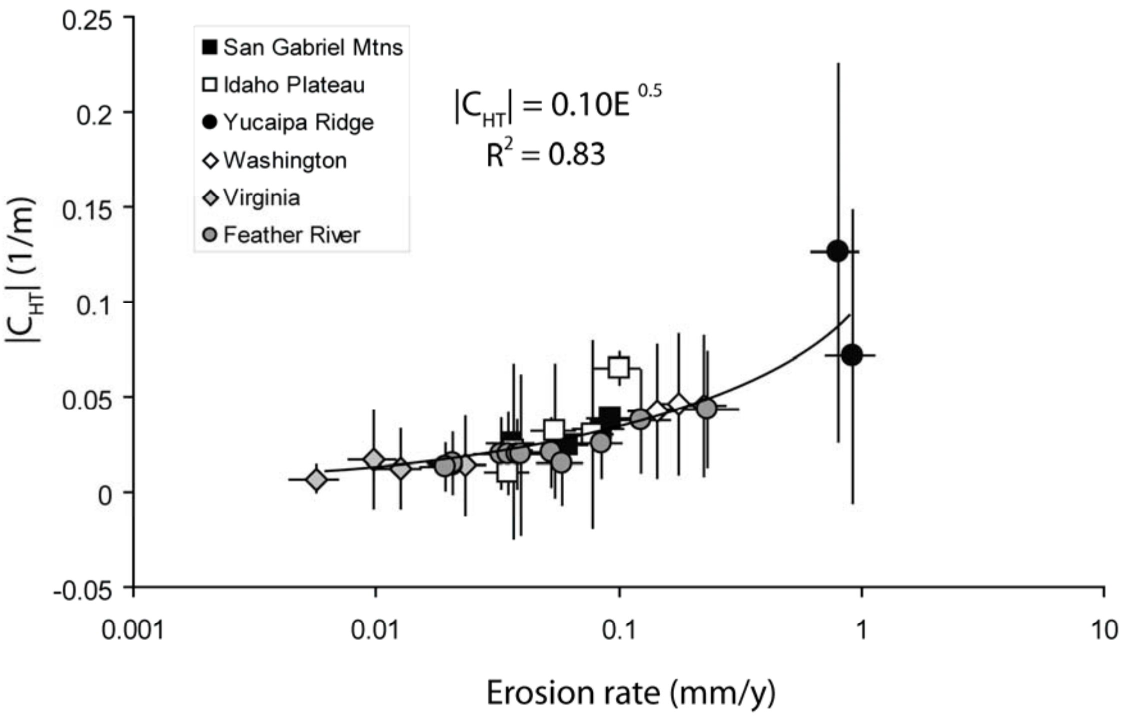

Figure 3. Ridgetop curvature increases with the square root of erosion rate (E). Because ridgetops have negative curvature, the absolute value of curvature is plotted to allow a power-law regression. Error bars along the x-axis represent analytical error (from AMS measurements) and uncertainties in production scaling and shielding [*Mudd et al.*, 2016]; error bars along the y-axis represent the median absolute deviation. Data plotted on semi-log axes to accommodate negative values. Various functions were tried for the regression; the power function yielded the highest R^2. Excluding the data from Yucaipa Ridge, where Eqn. 1 may not be strictly applicable because of steep slopes and an incomplete soil cover, does not change the regression equation (represented by the thick line).

(A)

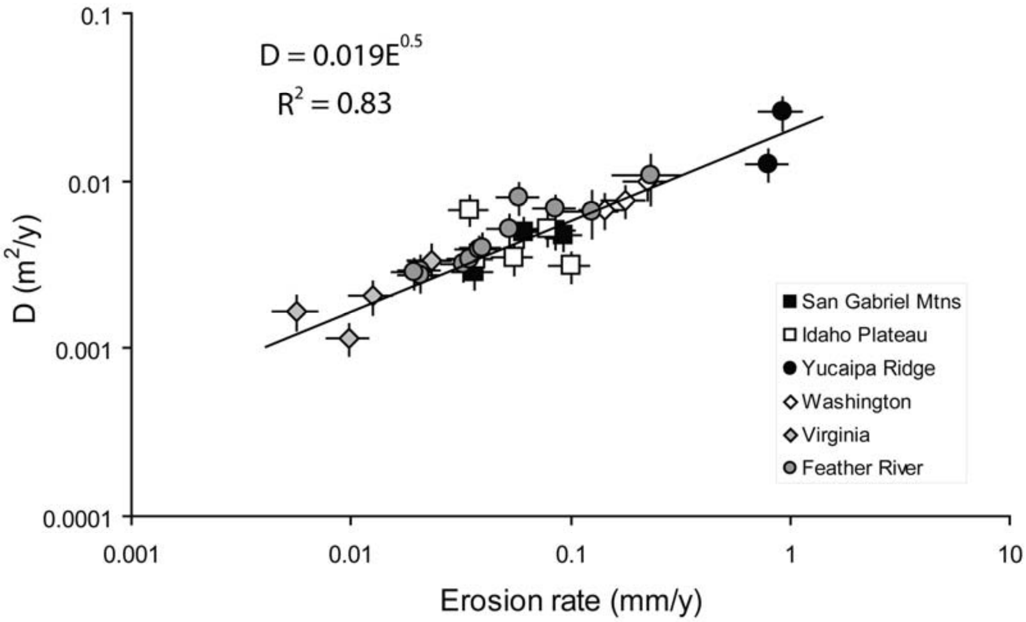

Figure 4. Transport efficiency increases with the square root of erosion rate. This relationship integrates the different factors that influence *D*, including soil thickness and particle size. Straight line is a plot of the regression equation. Error bars along the x-axis represent both analytical error (from AMS measurements) and uncertainties in production scaling and shielding [*Mudd et al.*, 2016]; error bars along the y-axis represent propagated uncertainties from erosion rate and curvature measurements.

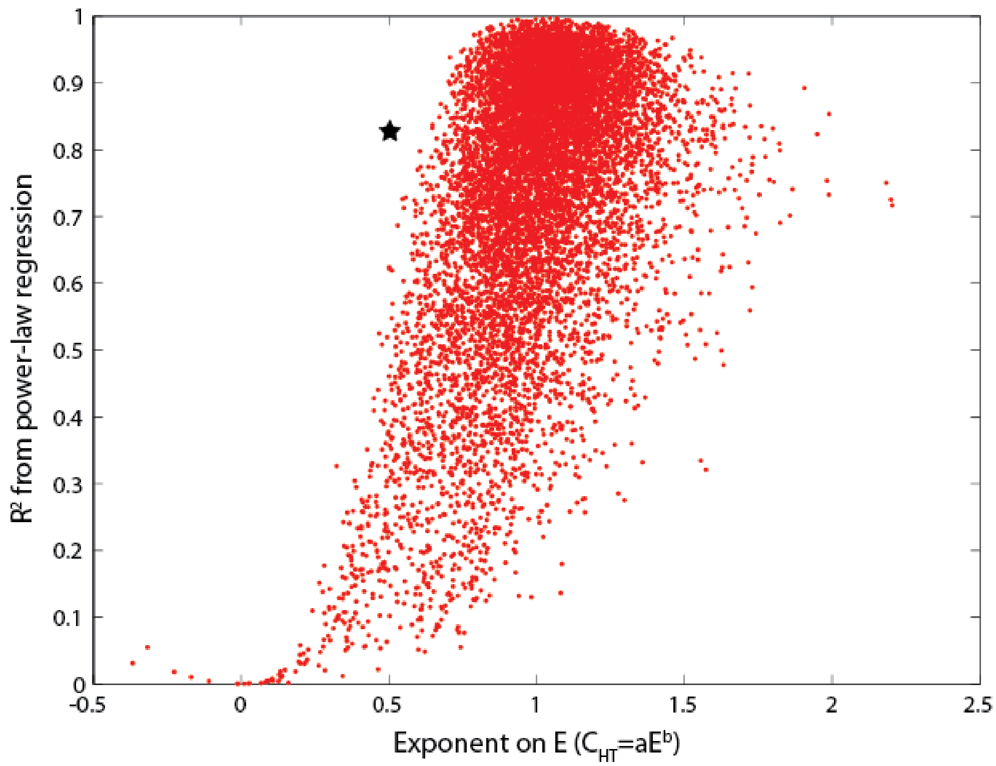

Figure 5. Results from 10,000 Monte Carlo simulations. Each red dot represents the outcome of a single simulation in which a power-law regression was fit to synthetic data. The black star represents the exponent and R^2 of the regression between ridgetop curvature on erosion rate from the actual data (Figure 3). The regression results from the actual data lie well outside the results from the simulations.

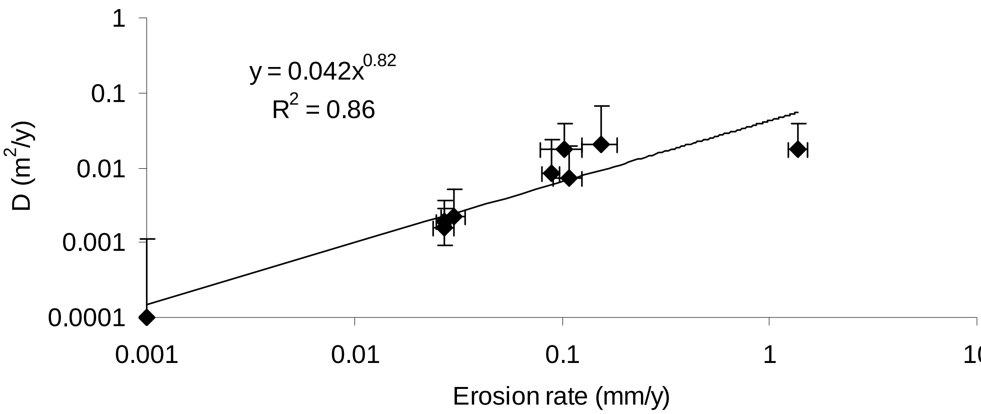

Figure 6. Transport efficiency vs. erosion rate using data from Richardson et al. [2019]. Error bars represent 1σ uncertainty.

Table 1. Site information.

Region	Sample ID	Latitude (°N)	Longitude (°W)	Lithology	MAT [i] (°C)	MAP [i] (mm)	Aridity Index	Eros. rate (mm/y)	Curvature (1/m)	D (m^2/ky)
San Gabriel Mountains (CA)[a]	SG128	34.3375	118.0104	granite	12	555	2037	0.0365	-0.02536	0.0029
	SG130	34.3782	117.9892	granite	11	598	2036	0.0849	-0.02470	0.0051
	SG131	34.3665	117.9919	granite	11	588	2029	0.0615	-0.03334	0.0050
	SG132	34.3658	117.9891	granite	11	601	2029	0.0925	-0.03902	0.0047
Idaho Plateau (ID)[b]	S1	45.4773	114.9618	tonalite	8	624	1167	0.0550	-0.03171	0.0035
	S2	45.5008	114.9518	tonalite	5	710	1141	0.1010	-0.06502	0.0031
	S3	45.5261	114.9292	tonalite	3	1166	1046	0.0370	-0.02150	0.0034
	R2	45.4842	114.9557	tonalite	7	618	1150	0.0780	-0.03012	0.0052
	R3	45.5345	114.9014	tonalite	2	1198	1034	0.0350	-0.01038	0.0067
Yucaipa Ridge	3	34.0496	116.9279	quartz monzonite, gneiss	9	701	2000	0.8008	-0.07159	0.0127
(CA)[c]	4	34.0530	116.9401	quartz monzonite, gneiss	9	701	2021	0.9215	-0.12596	0.0257
Olympic Peninsula (WA)[d]	U-WC-S	47.7399	124.0456	graywacke	8	3151	815	0.1768	-0.04624	0.0076
	L-WC-S	47.7302	124.0379	graywacke	8	3151	823	0.2249	-0.04525	0.0099
	L-EFMC-S	47.6581	124.2432	graywacke	9	1075	814	0.1435	-0.04243	0.0068
Blue Ridge Mountains (VA)[e]	SH-01a	38.5713	78.2872	granite	11	1075	1250	0.0232	-0.01378	0.0034
	SH-02a	38.6636	78.3550	metabasalt	10	1045	1223	0.0057	-0.00682	0.0017
	SH-07	38.5815	78.4143	granite	10	1086	1215	0.0099	-0.01710	0.0012
	SH-10	38.6572	78.2821	granite	12	1400	1227	0.0126	-0.01222	0.0021
Feather River (CA)[f, g, h]	BRB-2	39.6491	121.3020	quartz diorite	13	1332	1752	0.0327	-0.02028	0.0032
	BEAN-1	39.6126	121.3295	quartz diorite	14	1240	1828	0.0348	-0.02022	0.0034
	BEAN-2	39.6225	121.3283	quartz diorite	12	1361	1810	0.0381	-0.01978	0.0039
	BEAN-4	39.6237	121.3273	quartz diorite	12	1365	1810	0.0529	-0.02065	0.0051
	BEAN-5	39.6312	121.3298	quartz diorite	13	1347	1786	0.0395	-0.01971	0.0040
	BEAN-7	39.6284	121.3277	quartz diorite	11	1248	1786	0.0854	-0.02519	0.0068
	FT-3	39.6714	121.3109	quartz diorite	11	1237	1683	0.0208	-0.01420	0.0029
	FT-4	39.6712	121.3109	quartz diorite	10	1198	1683	0.0206	-0.01498	0.0027
	FT-6	39.6784	121.3155	quartz diorite	8	1219	1658	0.0193	-0.01349	0.0029
	SB-1	39.7189	121.2411	quartz diorite	15	1405	1695	0.0583	-0.01469	0.0079
	FR-4	39.6344	121.2770	quartz diorite	15	1405	1818	0.2335	-0.04335	0.0108
	FR-5	39.6354	121.2712	quartz diorite	12	1400	1792	0.1242	-0.03747	0.0066

[a] Source for ^{10}Be data and lithology: (DiBiase et al., 2010)

[b] Samples were collected for this study; source for lithology: (Wood, 2013)

[c] Source for ^{10}Be data and lithology: (Binnie et al., 2007)

[d] Source for ^{10}Be data and lithology: (Belmont et al., 2007)

[e] Source for ^{10}Be data and lithology: (Duxbury, 2009)
[f] Source for ^{10}Be data for all Feather River samples except FR-4 and FR-5: (Hurst et al., 2012)
[g] Source for ^{10}Be data for FR-4 and FR-5: (Riebe et al., 2001)
[h] Source for lithology: (Saucedo and Wagner, 1992)
[i] MAT = mean annual temperature; MAP = mean annual precipitation; data from the PRISM Climate Group, http://prism.oregonstate.edu, accessed 25 March 2017

Table 2. Details of ^{10}Be analysis from Idaho site.

Sample ID	Sample depth intervals (cm)	AMS measurement ID	^{10}Be concentration ($x10^3$ at g^{-1})	^{10}Be concentration uncertainty 1σ ($x10^3$ at g^{-1})
S1	0 - 2	s04446	119.9	5.7
S2	8 - 10	s04447	91.94	7.18
S3	16 - 18	s04448	373.7	17.8
R2	n/a	s04450	91.49	4.43
R3	n/a	s04451	408.8	15.1
R4	n/a	s04452	480.1	16.6